Materials Chemistry and Physics 351 (2026) 132010

Contents lists available at ScienceDirect

Materials Chemistry and Physics

journal homepage: www.elsevier.com/locate/matchemphys

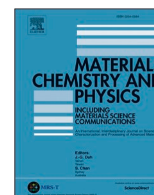

Phase engineering in NaNbO3 thin films fabricated by PLD: Strain, substrate and temperature role on the Q FE – P AFE phase transition

Olga Krymskaya [a,b,c,*], Pasquale Orgiani [d], Louis Muse [e], Jean-François Blach [e], Simone Sanna [c], Daniele Di Castro [c], Paolo Barone [b], Marco Fortunato [a], Rachel Desfeux [e], Carmela Aruta [b], Antonello Tebano [c]

[a] Department of Astronautical, Electrical and Energetic Engineering, CNR-SPIN, University of Rome "La Sapienza", 00185 Rome, Italy
[b] CNR-SPIN, via del Fosso del Cavaliere 100, 00133 Rome, Italy
[c] Department of Civil Engineering and Computer Science,University of Rome "Tor Vergata", Rome, Via del Politecnico 1 and CNR-SPIN, 00133 Rome, Italy
[d] TASC Laboratory in Area Science Park, CNR-Institute of Materials (IOM), Trieste 34139, Italy
[e] Univ. Artois, CNRS, Centrale Lille, Univ. Lille, UMR 8181, Unité de Catalyse et Chimie du Solide (UCCS), F-62300 Lens, France

HIGHLIGHTS

- Q.→P transition in NNO films at 600 °C occurs between 16 and 45 nm on NGO (110).
- On NGO (101), temperature enables pure Q or pure P films growth.
- At 750 °C Q relaxes faster and P nucleates giving unique AFM textures on NGO and STO.
- c-AFM reveals local I–V behavior in Q and P regions below and above 125 nm on STO.
- Raman and EIS confirm macroscopic FE and AFE below and above the given thresholds.

GRAPHICAL ABSTRACT

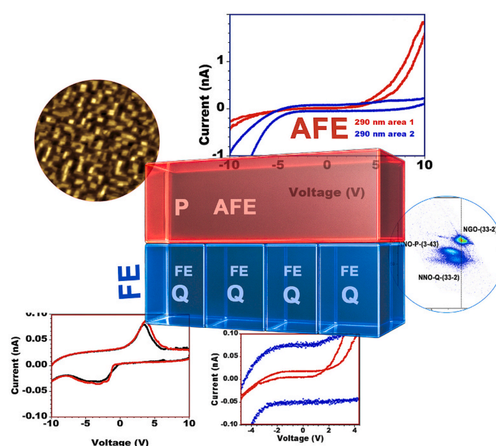

ARTICLE INFO

Keywords:
Sodium niobate ($NaNbO_3$)
Epitaxial thin films
Ferroelectric–antiferroelectric transition
Strain engineering
Pulsed laser deposition
X-ray diffraction

ABSTRACT

This study explores precise control over ferroelectric (Q) and antiferroelectric (P) phase transitions in $NaNbO_3$ (NNO) thin films, essential for sustainable electronic applications. Epitaxial NNO layers (10–290 nm) were grown via Pulsed Laser Deposition (PLD) onto $SrTiO_3$ (001) and $NdGaO_3$ (110)/(101). X-ray diffraction and reciprocal-space mapping show films deposited at 600 °C nucleate as a fully strained Q phase; beyond a thickness of about 45 nm on $NdGaO_3$, they relax into the P phase. Elevated deposition temperature (750 °C) facilitates early partial relaxation of the Q-phase and promotes nucleation and growth of the P-phase, evident from distinctive morphologies observed by Atomic Force Microscopy (AFM). Conductive AFM further links structural phases to their distinct electrical signatures, showcasing ferroelectric hysteresis in Q-phase regions and more complex loops in

* Corresponding author. Department of Astronautical, Electrical and Energetic Engineering, CNR-SPIN, University of Rome "La Sapienza", 00185 Rome, Italy.
E-mail address: olga.krymskaya@uniroma1.it (O. Krymskaya).

https://doi.org/10.1016/j.matchemphys.2026.132010
Received 3 September 2025; Received in revised form 22 December 2025; Accepted 1 January 2026
Available online 2 January 2026
0254-0584/© 2026 The Authors. Published by Elsevier B.V. This is an open access article under the CC BY license (http://creativecommons.org/licenses/by/4.0/).

P/Q mixed-phase domains. Notably, on $NdGaO_3$ (101), we demonstrate distinct single-phase growth; by selecting deposition temperature, we obtain exclusively the Q or P phase, without mixed states. These results provide insights into controlling structural transitions in NNO thin films, guiding their future development for sustainable electronics, energy storage, piezoelectric microdevices, and multifunctional systems.

1. Introduction

NNO possesses a very complex structural phase diagram. The different structural phases are associated with transitions from antiferroelectric (AFE) to ferroelectric (FE) to paraelectric phase. These phase transitions are generally temperature dependent, but at fixed temperature, the NNO phase transitions can be induced by multiple factors such as compositional modifications [1,2], external electric field applied [3,4], epitaxial strain [5,6], grain size [3,7], and chemicals utilized during the NNO preparation precursors [8–10]. While this general framework makes NNO one of the most structurally complex perovskites, it also makes NNO of great interest for its various potential applications in piezoelectric devices [11,12], photocatalysis and photoelectrochemical (PEC) water splitting efficiency [13–15], optoelectronics [16,17], cancer [18–20] and cardiovascular diagnostics [21,22] and biosensors [23], ultrahigh capacity storage devices [24–28].

Neutron diffraction studies [29–32] demonstrated that room-temperature NNO is not single phase but a mix of two symmetry-distinct polymorphs which result to be the most interesting for thin-film engineering today: the orthorhombic AFE P-phase (*Pbcm*) is characterized by lattice parameters $a_P = 5.566$ Å, $b_P = 15.52$ Å, $c_P = 5.506$ Å [30], the polar FE Q-phase ($Pmc2_1$), on the other hand, has lattice parameters $a_Q = 5.55$ Å, $b_Q = 5.63$ Å, $c_Q = 7.86$ Å [29,31]. Htet et al. [32] tracked the temperature dependence, showing that the Q-fraction decreases steadily from roughly 50 % at 25 °C to ≈ 16 % at 300 °C, while Zhang M.et al. linked slight Na/O non-stoichiometry to a measurable shift of the same balance [25]. Dimensional confinement seems to push in the opposite direction: freestanding membranes thinner than 40 nm are purely ferroelectric switching then into a mixed-phase state with coexistence of ferroelectric and antiferroelectric orders once this thickness is exceeded, as reported by Xu et al. [33].

Epitaxial NNO growth is highly sensitive to substrate orientation, deposition conditions, Na volatility, and strain, which together control domain structure and remanent polarization. The first study on NNO films deposited by PLD by Saito et al. [34] showed that epitaxial $NaNbO_3$ films grown on $SrTiO_3$ can be stabilized in a ferroelectric state, with clear P–E loops despite the bulk antiferroelectric ground state. Yamazoe et al. [35] then demonstrated that the $SrTiO_3$ substrate orientation strongly affects surface morphology and ferroelectric switching. Maeng et al. [36] used a single-crystal Rh substrate to impose a strong tetragonal strain and obtain very large remanent polarization. Sellmann et al. [37] subsequently mapped how oxygen pressure and Na non-stoichiometry control strain state and domain formation on different perovskite substrates, and Schneider et al. [38] showed that strain engineering can preserve the antipolar ground state while producing large switchable polarization and high energy-storage potential. (For the detailed PLD conditions see Supplementary information, Table S1).

Therefore, at room temperature, the polar Q-phase and antipolar P-phase compete both in bulk and in thin films. The antipolar octahedral NbO_6 tilt (Φ) favours the P-phase, while the polar displacement (P) defines the Q-phase.

The study of the free energy density in thin films as a function of misfit strain, conducted by Pertsev et al. [39], showed that epitaxial strain can strongly modify strain–temperature phase diagrams and can even induce ferroelectricity in films strained by the substrate. This is consistent with the observation that the ferroelectric Q phase forms in the first layers of NNO deposited onto substrates with compressive strain imposed. For the NNO thin films, the first-principles maps created by Patel et al. indicate a narrow monoclinic region under moderate strain [40], but in real films, relaxation with thickness drives the structure back to the antipolar phase. Within this framework, even modest changes in strain and thickness are expected to displace NNO films between ferroelectric- and antiferroelectric-like branches of the same free-energy surface. The exact transition point and its dependence on growth temperature and substrate orientation remain unclear.

We explore for the first time the combined interplay of multiple deposition parameters in stabilizing the Q and P phases of NNO. While previous studies have examined these factors only in isolation, our work adopts a more comprehensive approach by realizing, via PLD, four complementary series of epitaxial films.

1. *Temperature series on $NdGaO_3$ (110).* 120 nm thick films grown at 600 °C and 750 °C in order to test the differences in Q phase evolution before it transfers to the P.
2. *Thickness series on $NdGaO_3$ (110).* Films with thicknesses from 10 nm to 300 nm grown at 750 °C in order to trace the Q-to-P transition and surface structures evolution.
3. *Strain contrast.* 120 nm thick films grown on $NdGaO_3$ (110) (compressive) and $SrTiO_3$ (001) (near-matched) in order to isolate elastic effects at fixed temperature.
4. *Orientation contrast.* 120 nm thick films on $NdGaO_3$ (101) and $NdGaO_3$ (110) grown side-by-side at 750 °C reveal how lattice tilt relative to the polar axis steers the phase outcome.

Reciprocal-space maps and θ – 2θ scans track changes in the Q-to-P cell unit's out-of-plane vs in-plane orientation. Tapping-mode AFM and conductive-AFM (c-AFM) couple surface structures to local current–voltage loops, directly linking domain texture to crystal structure. Raman and impedance spectroscopy confirm changes in the crystal structure and, therefore, the macroscopic physical properties.

2. Experimental methods

2.1. NNO thin films preparation

The NNO thin films were prepared by PLD. The NNO target was prepared by solid-state reaction. The prepared target was utilized in a vacuum chamber for the PLD of NNO thin films. The deposition was performed with varying partial oxygen pressure from 10^{-2} mbar–1 mbar to optimize the deposition conditions. The substrate temperature was held at 600 °C and 750 °C during deposition to investigate the temperature's influence on the crystallographic quality of the films. In this study, 1.4 % Nb-doped STO (Nb-STO) (001) and $NdGaO_3$ with (110) and (101) orientations, hereafter referred to as STO and NGO, respectively, were employed to investigate how different substrate, because of the lattice matching, surface energy and symmetry, influence the growth, microstructure, and properties of the deposited thin films. Structural characterization (θ–2θ and RSM) were performed on films grown on insulating NGO substrates as stated in each series in Results and Discussion. Conductive 1.4 % Nb:STO was used only for c-AFM measurements to provide a conductive bottom contact; Nb doping is confined to the substrate and does not modify the PLD growth recipe.

For the further details see Supplementary Information.

2.2. Misfit evaluation

To estimate the lattice mismatch among STO, NGO, and the P and Q

phases of NNO, we refer to their respective pseudocubic unit cells. The in-plane misfit strain was computed as

$$\varepsilon = \frac{(a_{sub} - a_{film)}}{a_{film}}$$

along the two orthogonal substrate axes. For NNO, we adopt, a pseudocubic (p_c) unit cell derived from the real lattice parameters reported by Hewat [30] and Ahtee and Hewat [31]. The orthorhombic AFE P-phase lattice parameters can be expressed in terms of a quadrupled pseudocubic cell. The polar FE Q-phase ($Pmc2_1$) cell on the other hand, corresponds to a doubled pseudocubic cell. The resulting pceudocubic lattice parameters are:

- AFE P phase ($Pbcm$) → ($a^P_{pc} = a^P/\sqrt{2} = 3.9358$ Å, $b^P_{pc} = b^P/4 = 3.879$ Å, $c^P_{pc} = c^P/\sqrt{2} = 3.8933$ Å);
- FE Q phase ($Pmc2_1$) → ($a^Q_{pc} = a^Q/\sqrt{2} = 3.9244$ Å, $b^Q_{pc} = b^Q/\sqrt{2} =$ 3.981 Å, $c^Q_{pc} = c^Q/2 = 3.93$ Å).

The substrate in-plane lattice parameters are: for STO(001)$a_{STO} = b_{STO}$ = 3.905 Å, for NGO(110)$a_{NGO(110)} = 3.863$ Å, $b_{NGO(110)} = 3.854$ Å, for NGO(101)$a_{NGO(101} = 3.889$ Å, $b_{NGO(101)} = 3.853$ Å.

The resulting per-axis misfits are tabulated in Supplementary Information Table S2 (reported as ε_a, ε_b).

2.3. Structural, morphological and electrical characterization

The films were characterized by X-ray diffraction (XRD) and reciprocal space mapping (RSM) to determine their crystallographic quality, structure and strain state, by atomic force microscopy (AFM) and conductive AFM (c-AFM) to probe surface morphology and local electrical behaviour, by Raman spectroscopy on selected NNO/STO samples to refine the Q/P phase assignment, and by low-field impedance measurements to obtain an effective permittivity for representative films. Conventional θ–2θ scans and rocking curves were recorded on a Rigaku diffractometer equipped with a Co anode, emitting radiation with wavelength λ = 1.78901 Å, operated at 30 kV and 30 mA. High-resolution RSMs were acquired on a Malvern Empyrean four-circle diffractometer with a Cu anode (40 kV, 30 mA), a double-bounce 2 × Ge(220) hybrid monochromator providing the Cu $K\alpha_1$ (1.54060 Å) wavelength only, and a GaliPIX3D detector with an active area of 481 × 465 pixels (equatorial and axial angular windows of 6.8898° and 5.7632°, respectively).

AFM and c-AFM measurements (Nanosurf CoreAFM) were used to analyse the surface topography and local conductive properties of the NNO films. Topography was recorded in tapping mode with an Al-coated cantilever (190 kHz, 48 N/m, 225 μm). Local conductive measurements were performed in contact mode with a cantilever (75 kHz, 3 N/m, 225 μm) coated with 5 nm Cr and 25 nm Pt on both sides.

Raman spectroscopy experiments were carried out on NNO/STO films using an Xplora Plus (Horiba) spectrometer equipped with a 532 nm laser line to further characterise the structural properties, in particular the presence of the FE Q phase and the emergence of the AFE P phase. For each sample, three spectra were collected on different surface regions by focusing the beam on areas of a few μm^2 to check reproducibility. The recorded spectra were processed by first subtracting the STO contribution, achieved by subtracting the spectrum of a bare STO substrate acquired under identical conditions. The resulting spectra, which exhibited very broad bands, were then deconvoluted using the LabSpec software.

Temperature-dependent impedance measurements were performed using a Solartron impedance analyser controlled by MTS software. The real and imaginary components of the impedance (Z' and Z'') were recorded as a function of temperature at 1 kHz with an AC excitation amplitude of 10 mV. An effective capacitance was obtained from the imaginary part of the impedance at this frequency, and the corresponding relative permittivity was then obtained.

3. Results and Discussion

The XRD pattern of NNO thin films, with thicknesses ranging from 16 to 200 nm, deposited on an NGO (110) oriented substrate at 600 °C and an oxygen partial pressure of 1 mbar, clearly confirms that the films are highly oriented. Notably, no spurious phases are present, and only peaks corresponding to a single crystallographic orientation are observed (Fig. 1a). The X-ray diffraction pattern of the 16 nm-thick film (Fig. 1a, blue line) displays two peaks at 2θ = 26.0° and 53.6°. In contrast, thicker films (45, 125, and 200 nm; green, red, and black lines, respectively) show these peaks shifted to higher angles, at 2θ = 26.4° and 54.4°, respectively. Such shifts in XRD angular positions with increasing thickness may arise either from relaxation of compressive strain or from the emergence of two distinct crystallographic phases coexisting at room temperature. The orthorhombic Q phase (a = 5.55 Å, b = 5.63 Å, c = 7.86 Å) [29,32] would produce the (110) and (220) reflections at 2θ = 26.16° and 53.83°, whereas the orthorhombic P phase (a = 5.57 Å, b = 15.52 Å, c = 5.50 Å) [30] would produce the (101) and (202) peaks at 2θ = 26.43° and 54.40°. Although symmetric XRD alone cannot unambiguously distinguish between these phases, the close agreement between experimental and calculated peak positions suggests that the 16 nm film crystallizes in the FE Q phase. In contrast, the 45, 125, and 200 nm films adopt the AFE P phase, as explained below.

The full width at half maximum (FWHM) values observed in the omega scan, around the reflection at 2θ = 54.4° for the 125 nm thick film, approximately 0.07°, further confirm the excellent structural quality of the films. Such narrow FWHM values are indicative of low mosaicity and reduced defect density (inset Fig. 1a). The deposition rate and, consequently, the film thickness were calculated based on the finite size Laue oscillations observed in the symmetric θ–2θ XRD pattern, of the 16 nm thick film showed in Fig. 1b). These results were confirmed by X-ray-reflectivity measurements (Fig. 1c). The observation of Laue oscillations indicates the high structural quality of the deposited films, demonstrating that the deposition parameters are optimized.

To investigate the in-plane structural relationship between the substrate and the NNO films as a function of the thickness, RSMs around the (33-2)-NGO asymmetric reflections were acquired. Fig. 1d and e displays two diffraction peaks, which, very likely, can be indexed as the NNO-Q-(33-2) and NNO–P-(3–43) reflections along with those of the NGO substrate. In the thinnest NNO film (Fig. 1d), a single diffraction peak is clearly visible, aligning with the Q_x direction, defined as the in-plane component of the scattering vector corresponding to the substrate's peak position, thus indicating that the observed NNO film, confidently assigned to the Q-phase, grows, at the earliest stage, fully strained with the substrate. As the thickness increases, a second diffraction peak, assigned to the NNO P-phase, appears with a different value of Q_x, indicating the mismatch in the in-plane lattice parameters of the substrate (Fig. 1e). Interestingly, regarding the Q-phase, there is no trace of a structural relaxation of this very strained phase. In fact, both the Q and P phases do not always show any change in the out-of-plane lattice parameter. Such behavior is also evident in the symmetrical θ–2θ scans, where only the relative intensities of the diffraction peaks change with film thickness, while their angular positions remain constant. Such a scenario is compatible with a sudden structural relaxation occurring at a critical thickness, which abruptly separates the interfacial fully-strained Q-phase from the P-phase relaxed one far from it.

To investigate the effect of temperature on the structural properties, further studies were conducted on NNO films, with different thicknesses, deposited on NGO (110) oriented substrate at temperature T = 750 °C and oxygen partial pressure P = 1 mbar.

Fig. 2a illustrates XRD θ-2θ patterns for films having thicknesses ranging from 22 to 290 nm. For films with thicknesses up to 80 nm, a single, distinct diffraction peak is observed at about 2θ = 26.4° and at higher 2θ angle around 54.5°. In this case, assuming for the Q and P

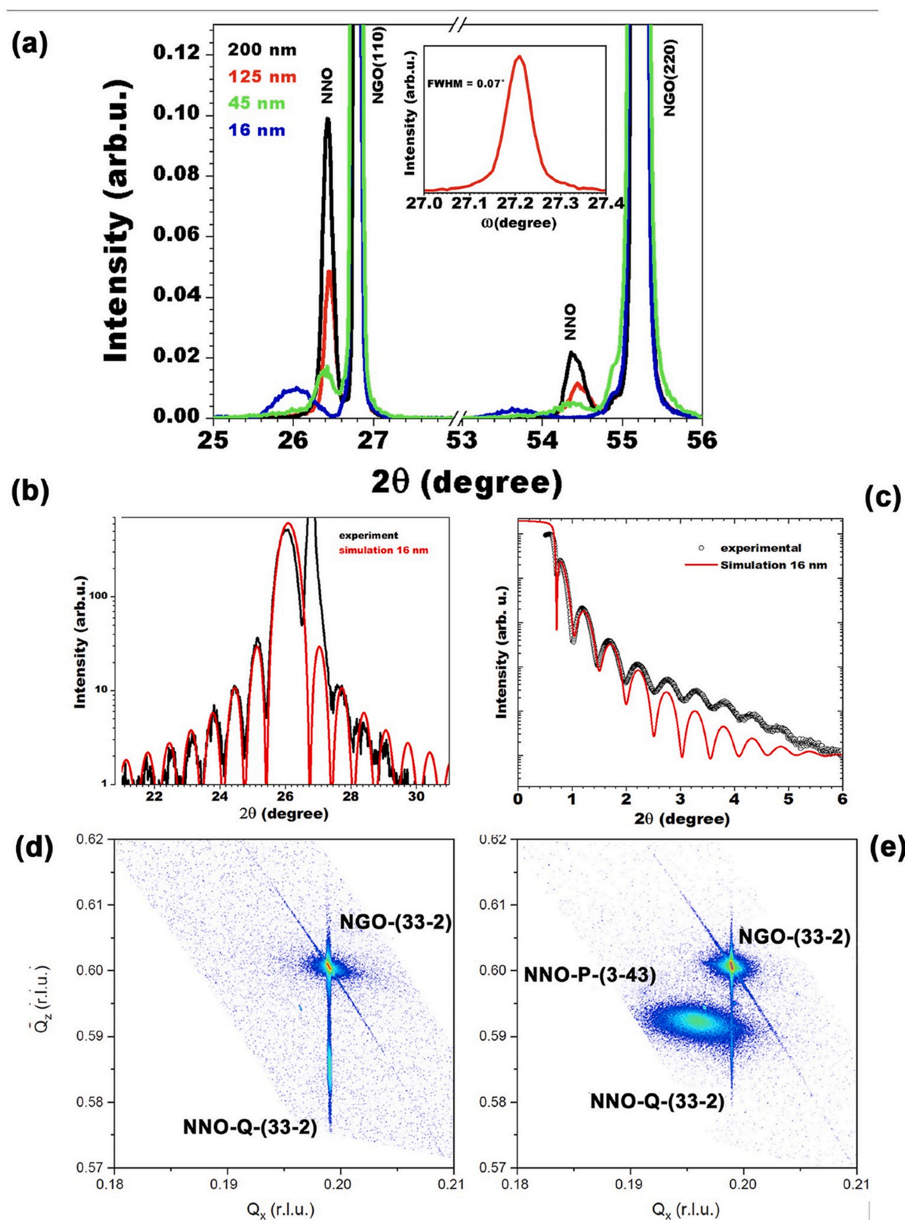

Fig. 1. X-ray diffraction study for NNO films deposited on NGO (110) substrates at 600 °C and oxygen partial pressure 1 mbar $\theta - 2\theta$ diffraction pattern, normalized to the substrate peak intensities as a function of thickness. In the inset the rocking curve around the NNO reflection at $2\theta = 54.5°$, for the film 125 nm thick. (b) Laue finite-size oscillations around the reflection at $2\theta = 26°$ and (c) X-ray reflectivity profile both experimental data (black dots) fitted by simulation (red curves). Reciprocal space maps around the NGO-(33-2) asymmetric reflection of the substrate refers to a 16 nm (d) and a 125 nm (e) NNO film thicknesses; in particular, NNO-Q(33-2) and NNO–P-(3–43) asymmetric reflections can be identified. (For interpretation of the references to color in this figure legend, the reader is referred to the Web version of this article.)

phases the previously mentioned orthorhombic unit cells, it is very likely to attribute the XRD peaks, observed for thinner samples, to the (110) and (220) reflections of the Q phase. For films with a thickness over 125 nm, specifically 290 nm, the P phase, characterised by the XRD peaks at $2\theta = 26.58°$ and $54.85°$, corresponding to the (101) and (202) reflections, becomes predominant. For the 50 nm and 80 nm thick films, it is possible to observe a shift, or a potential broadening of the diffraction peak toward higher 2θ angles compared to the peaks in the diffraction pattern of the 22 nm film. This behaviour indicates the possible early coexistence of the two phases that become clearly distinguishable in the diffraction pattern of the 125 nm film. The coexistence of these phases suggests either the onset of structural instability or a competitive interplay between them as the film thickness increases from 22 nm to 50 nm.

To better clarify the determination of the correct phase, namely Q or P, similarly to the analysis conducted for NNO samples deposited at 600 °C, RSMs were acquired as a function of film thickness for NNO films deposited at high temperature (750 °C), as reported in Fig. 2b–c.

Different from samples grown at lower temperature, the thinnest (22 nm) NNO film shows the presence of a diffraction peak well aligned along the in-plane scattering vector Q_x direction of the substrate's peak, along with an intensity profile spreading far from it. Such data indicate the presence of a structural relaxation process of the NNO Q-phase, originating at the film/substrate interface and extending up to a few tens of nanometers far from it. Again, for very thick films (290 nm), NNO P-phase has been observed to occur in a structurally relaxed way, with no in-plane matching with the lattice parameter of the substrates. As for the previous case, such a structural evolution of the NNO films as a function

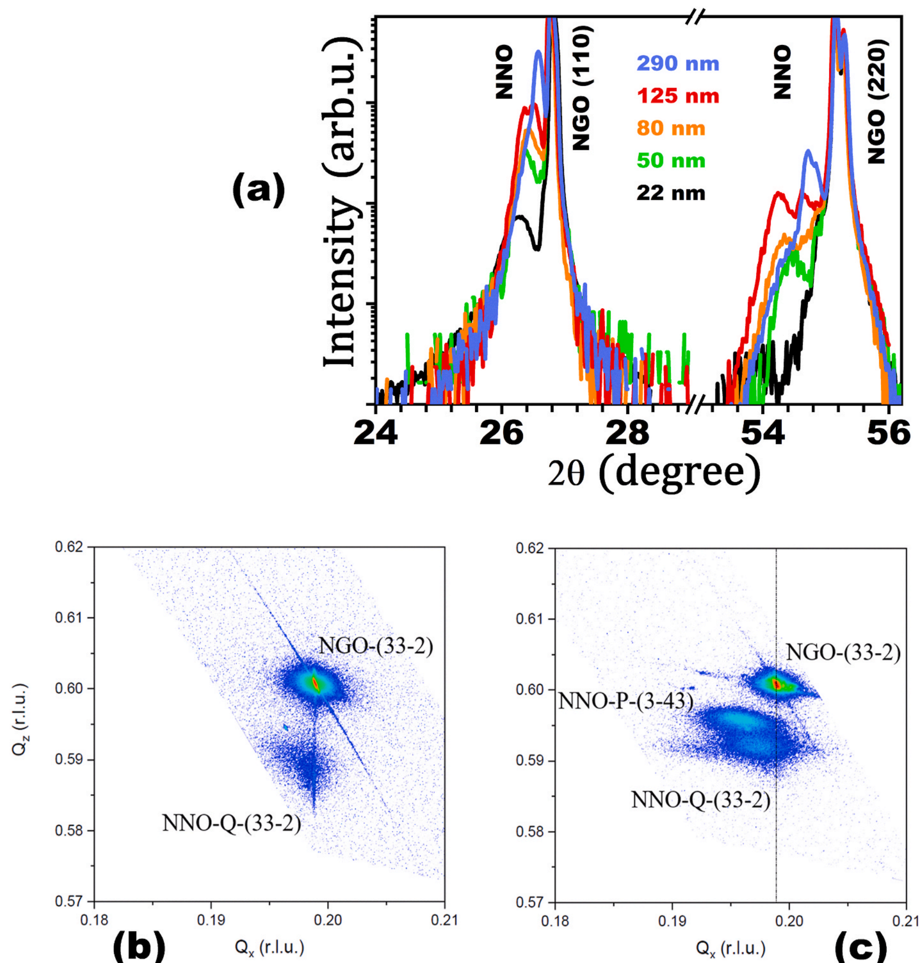

Fig. 2. X-ray diffraction study for NNO films deposited on NGO (110) substrates at 750 °C and oxygen pressure 1 mbar
$\theta - 2\theta$ diffraction pattern, normalized to the substrate peak intensities as a function of thickness ranging from 10 nm to 290 nm. Reciprocal space maps around the NGO (33-2) asymmetric reflection of the substrate refer to a 22 nm (b) and a 125 nm (c) NNO film thickness; in particular, NNO-Q(33-2) and NNO–P-(3–43) asymmetric reflections can be identified.

of the thickness is also visible in the symmetrical θ–2θ scans (Fig. 2a), where, in addition to the arising of second diffraction peaks (i.e. P phase), the diffraction peaks related to the interfacial Q phase are observed to shift to higher angles.

The whole set of data therefore indicates profound differences in the relaxation mechanism of NNO films grown at lower (600 °C) and higher (750 °C) temperatures. While in the first case, the NNO films appear to be formed by two independent, although structurally homogeneous, phases (i.e. fully strained Q phase and fully relaxed P phase), in the NNO films grown at higher temperature, the interfacial Q phase partially relaxes before being replaced by the relaxed P phase, which is confirmed to be typical of NNO films with higher thickness.

To clarify the XRD signatures of the P and Q phases, previously observed to vary with both film thickness and deposition temperature, we investigated their temperature-dependent growth behavior by also depositing films of 200 nm thickness on NGO(101) substrates. Fig. 3a presents the XRD patterns for films grown at 600 °C (blue line) and 750 °C (red line). The film grown at 750 °C exhibits two diffraction peaks at $2\theta = 47.0^\circ$ and 105.5°, which can be ascribed to the (042) and (084) reflections of the P phase. Theoretical 2θ positions for these reflections are 46.98° and 105.72°. The excellent agreement with the experimental values indicates that, at the deposition temperature of 750 °C, the P phase is predominant.

In contrast, the film deposited at 600 °C shows peaks at $2\theta = 46.5^\circ$ and 104.5°, which can be attributed, within experimental uncertainty, either to the (202) and (404) reflections of the Q phase or to the (240) and (480) reflections of the P phase, expected at 46.49° and 104.23° and 46.58° and 104.51° respectively. These findings indicate that the peaks appearing at higher temperatures are correlated, very likely, to the appearance of the AFE P phase. The two XRD peaks appearing in the films deposited at lower temperature can be correlated to the P phase with slightly different lattice parameters, because of different strain conditions induced by the deposition temperature, or to the Q phase.

In order to enlighten possible strain mechanisms at play in those NNO films deposited onto NGO (101) oriented substrate at 600 °C and 750 °C, RSMs were performed and are reported in Fig. 3b–c. Different from NNO films grown on (110)-oriented NGO, here the RMSs do show a single diffraction peak of the grown phase with no trace of a double-phase structure, nor of fully strained ones at the interface with the substrate. The two observed peaks belong to two different fully relaxed structures both at 600 °C and 750 °C.

At 600 °C, the strain for FE Q phase on NGO(101) is biaxially compressive, with $\varepsilon_a = -2.31$ % and $\varepsilon_b = -1.96$ %; for the AFE P phase the strain is also compressive, however, because its lattice parameters are closer to those of the substrate, the strain is lower, with $\varepsilon_a = -1.19$ % and $\varepsilon_b = -1.04$ % (see Supplementary information, Table S2). At lower growth temperature, the thickness for the appearance of the P phase becomes larger, allowing the elastic energy stored in the highly compressed strained layer to stabilize the FE Q phase during growth. Raising the deposition temperature to 750 °C enhances dislocation mobility and

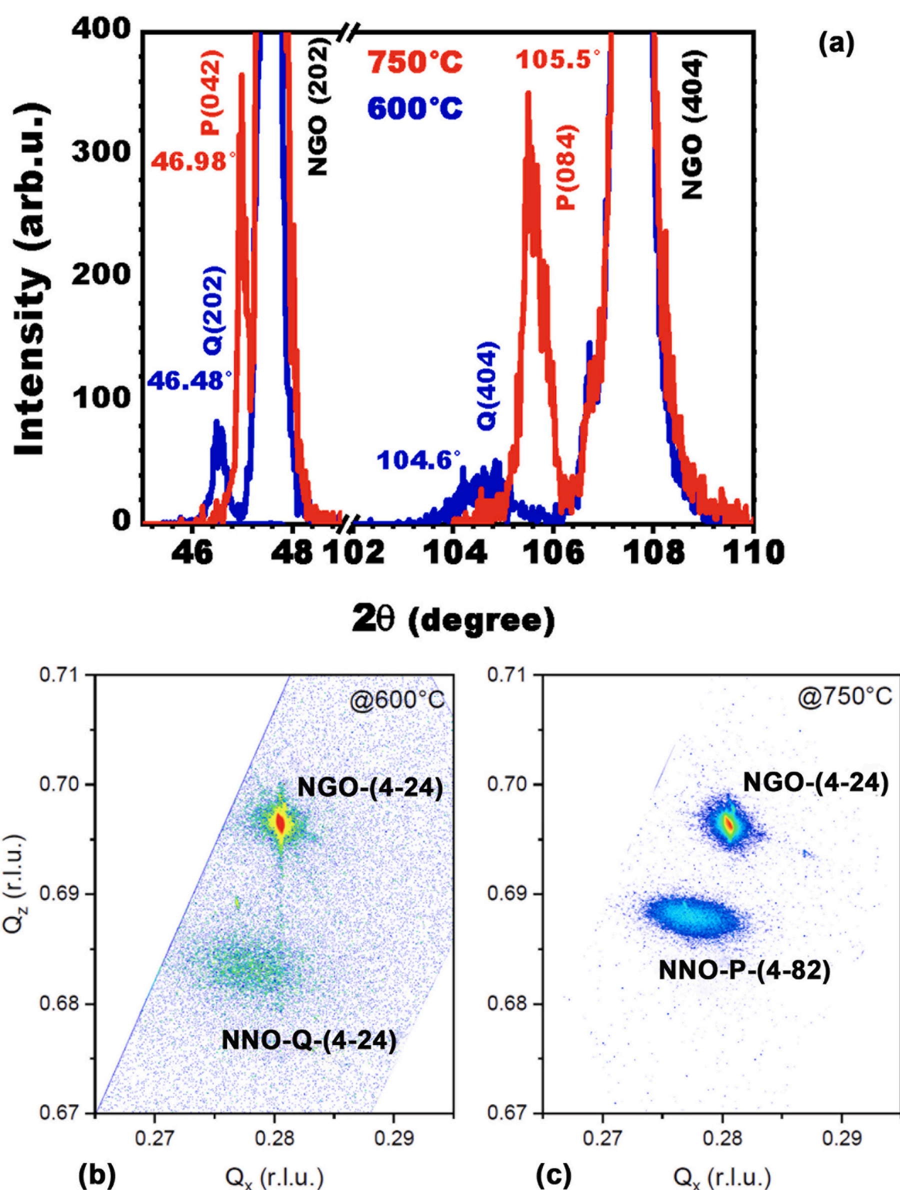

Fig. 3. X-ray diffraction study for 200 nm thick NNO films deposited on NGO (101) substrates at oxygen partial pressure 1 mbar
(a) $\theta - 2\theta$ diffraction pattern normalized to the substrate peak. The blue line corresponds to deposition at 600 °C and the red line to 750 °C. Reciprocal space maps around the NGO-(4–24) asymmetric reflection of the substrate, (b) samples grown at 600 °C and (c) at 750 °C; in particular, NNO-Q-(4–24) and NNO–P-(4–82) asymmetric reflections can be identified for the films. (For interpretation of the references to color in this figure legend, the reader is referred to the Web version of this article.)

enables partial relaxation already during deposition; as a result, the better-matching AFE P is favoured and a pure P film is obtained. This temperature lever on NGO(101), therefore, reflects a change from strained (Q) to relaxed (P) growth.

An AFM study of the morphology of NNO films deposited on (110)-oriented NGO substrate was conducted to gain deeper insight into the mechanisms governing this structural phase transition and the interplay between the two phases.

In Fig. 4, the tapping mode AFM topography images show the morphology of two films deposited at oxygen partial pressure 1 mbar and deposition temperatures 600 °C and 750 °C, Fig. 4a and b, respectively. Both samples have the same thickness of 125 nm, where Q and P phases are expected to coexist. However, the Q phase is likely to dominate at a growth temperature of 600 °C, while the P phase should prevail at 750 °C. The AFM analysis reveals significant differences in the surface morphology, which can be correlated to the structural features observed in the XRD scans. Despite the different types of grain morphology, which becomes more wrinkle- or boomerang-like in the NNO film grown at higher temperature, the surface root mean square roughness, obtained by Gwyddion based AFM measurements, resulted to be approximately 30–40 nm for both samples possibly related to the presence of the two distinct phases in XRD scans. As strain effects on the differing morphologies can be excluded, due to the use of the same substrate type and film thickness, the observed variations in morphology indicate that deposition temperature plays a crucial role in governing the film growth. These data support the XRD findings and highlight the influence of deposition temperature on phase formation and film growth mechanisms. In agreement with the XRD measurements discussed above, both NNO films are expected to exhibit coexistence of the Q and P phases. The different morphologies can be associated to the different strain conditions of the underlying layer: in the film grown at 600 °C, the Q phase is still strained when the P phase starts to appear at a thickness

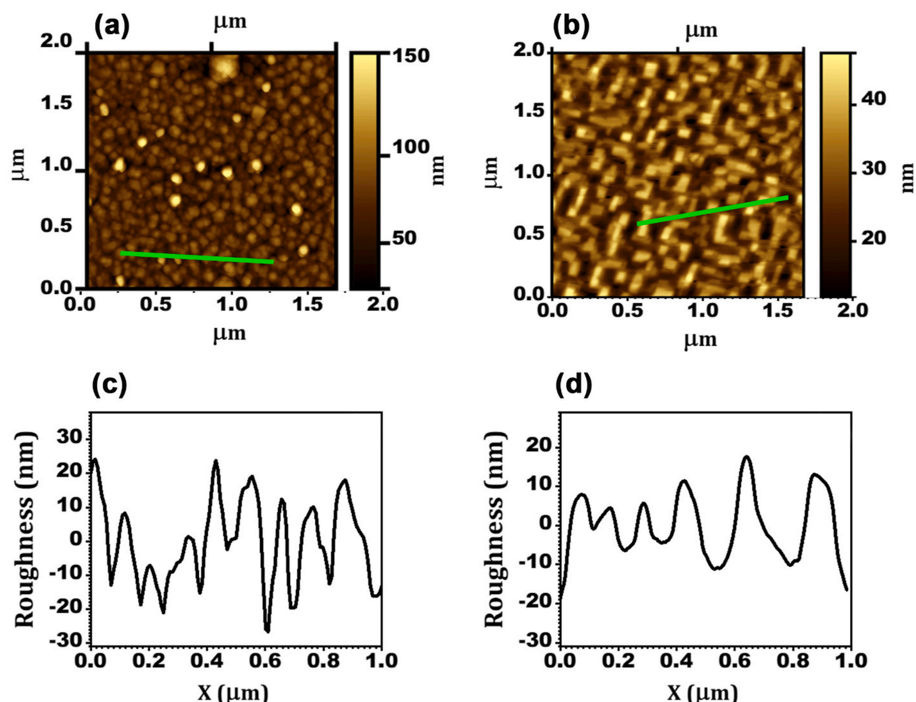

Fig. 4. AFM study on NNO films deposited on NGO (110) substrate
Tapping mode AFM topography images and roughness profiles of NNO films with a thickness of 125 nm, deposited on NGO (110) substrate at an oxygen partial pressure of 1 mbar and at the deposition temperatures of 600 °C (a, c) and 750 °C (b, d), respectively.

of about 45 nm, whereas in the film grown at 750 °C, the Q phase is already relaxed when the P phase emerges at about 80 nm. The larger nanocrystal domains observed in Fig. 4 b can therefore be associated with the higher growth temperature, which stabilizes the formation of the Q relaxed phase at the interface with the substrate.

Further steps were taken to study the double-phase growth of NNO at a deposition temperature of 750 °C, excluding the strain influence induced by the substrate. The STO cubic cell, with a lattice parameter of 3.905 Å, closely matches the pseudocubic cell of NNO, which has a lattice parameter ranging from 3.89 to 3.92 Å. As a result, the diffraction peaks from the film and the substrate are nearly superimposed in conventional θ–2θ XRD scans, making it challenging to distinguish the film peak from that of the substrate.

To better understand the role of the substrate, within the same deposition run, STO (001) and NGO (110) substrates (the one shown in Fig. 4), both approximately 3 × 3 mm^2 in size, were placed side by side on the sample holder. Under these conditions, the deposition parameters for the two films grown on these substrates can be considered identical. This is supported by the fact that PLD generally produces samples with a high degree of surface homogeneity over areas around 10 × 10 mm^2. This procedure ensured the resulting films differed only in the substrate used.

Fig. 5 demonstrates the tapping mode AFM topography of the samples deposited onto STO substrate at 750 °C and 1 mbar of oxygen partial pressure (Fig. 5 a and 5 c for the 125 nm thickness and Fig. 5 b and 5 d for the 290 nm), respectively. While the 125 nm thick film grown on NGO (Fig. 4b–d) presents "light" 3D structures approximately 20 nm high on the underlying "dark" layer, its twin-film on STO (Fig. 5a) results in almost a flat, "dark" surface, represented in blue rectangle. The overall roughness of 2 nm is essentially due to the presence of "light" points. In Fig. 5c, the roughness profile was obtained on the line crossing the "light" points (Fig. 5a, white rectangle). Moving to the 290 nm thick film on STO, we observe the regular "light" structures (Fig. 5b, white rectangle), similar to those of 125 nm thick film grown on NGO (Fig. 4 b), where the two P and Q phases are expected, while the underneath areas are of "dark" color (Fig. 5 b, blue rectangle). For this film, the roughness, measured along the green line (Fig. 5 b), is reported in Fig. 5 d and results in about 50 nm. Moreover, for the 125 nm STO sample, the "light" points (Fig. 5a, white rectangle) very likely represent the nucleation seeds of the P phase grown on the smoother surface of the Q phase. For films of comparable thickness, where we observed the appearance of nucleation seeds, Schneider et al. [6] reported the emergence of an additional reflection in the XRD pattern for 130 nm-thick samples deposited on STO at 750 °C. Considering that on STO (001) the FE Q misfit is modest (−1.91 %/−0.49 %) (see Supplementary materials Table 2), relatively to NGO(110), the Q→P transition occurs at a higher thickness (~120–130 nm). In addition, switching from Q to P phase reverses the sign on one in-plane axis (AFE P: −0.78 %/+0.30 %), so further relaxation is required before the P phase becomes energetically favorable, thus reinforcing the delayed transition on STO.

To independently confirm the emergence of the AFE P phase on STO as the film becomes thicker, we performed Raman spectroscopy on NNO films with thicknesses of 100 nm and 150 nm, grown at 750 °C on STO substrate. These thicknesses were chosen on either side of the FE–AFE crossover on STO, which, as discussed below, occurs for thicknesses slightly above 125 nm. Fig. 5e and f shows the corresponding Raman spectra. The spectra display the broad bands characteristic of $NaNbO_3$, in good agreement with previous Raman studies on $NaNbO_3$ in different forms [41,42], together with some residual features from the STO substrate. Group-theory analysis indicates that both the Q and P structures give rise to many Raman-active modes, most of which are common to the two phases and therefore not phase-selective. A notable exception is the band around 600 cm^{-1}, assigned to the ν_1 stretching mode of the NbO_6 octahedra, whose position is known to depend on the phase: in $NaNbO_3$ it typically appears at 610–620 cm^{-1} in the FE Q phase and 598–605 cm^{-1} in the AFE P phase [41,42]. In our films, this mode is centred at 611 cm^{-1} for the 100 nm sample (Fig. 5e) and at 598 cm^{-1} for the 150 nm sample (Fig. 5f). This behaviour is consistent with a FE Q-like structure at 100 nm and an AFE P-dominated structure for thicknesses above 125 nm on STO, and provides an independent confirmation of the thickness-driven evolution from FE to AFE character inferred from XRD and AFM.

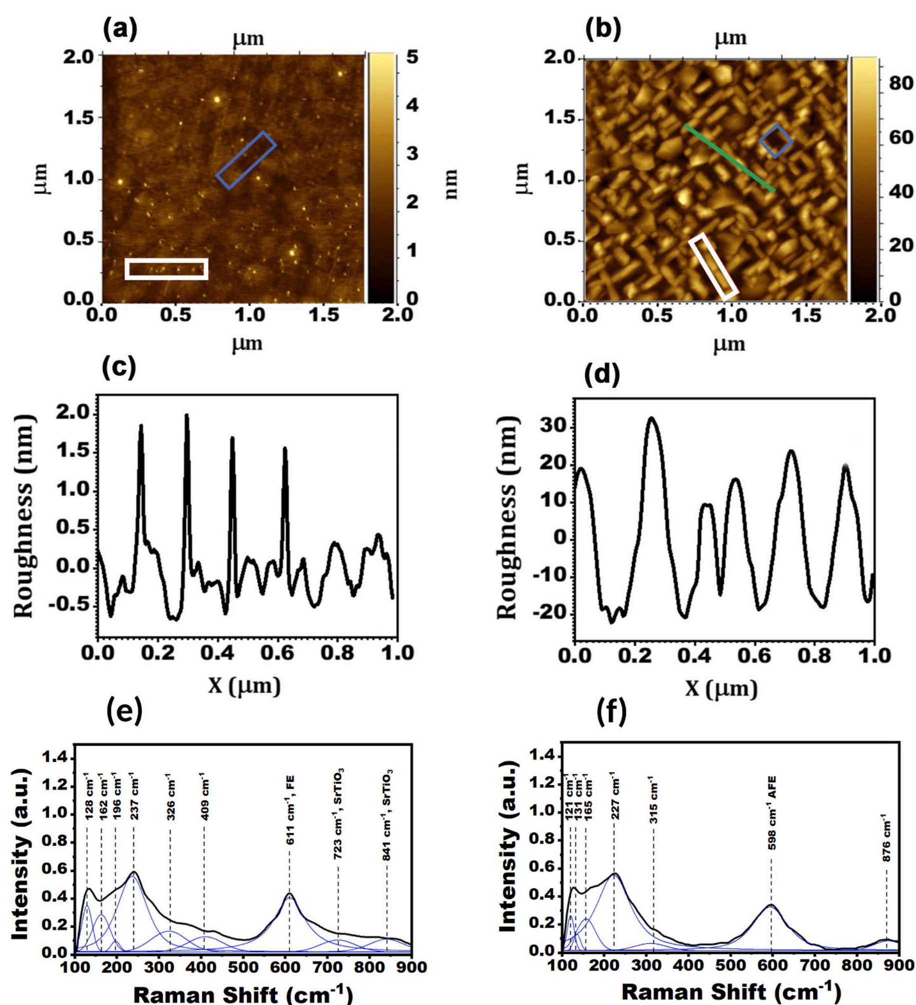

Fig. 5. AFM study and Raman spectroscopy on NNO films deposited on STO (001) substrate
Tapping mode AFM topography images with roughness profiles and experimental Raman spectra of NNO films, deposited on STO (001) substrate at an oxygen partial pressure of 1 mbar at the temperatures of 750 °C with thicknesses of 125 nm (a, c, e) and 290 nm (b, d, f) respectively. The blue curves correspond to the individual vibrational modes obtained through spectral deconvolution of the Raman spectra (black lines). (For interpretation of the references to color in this figure legend, the reader is referred to the Web version of this article.)

In order to investigate the correlation between the morphology and local electrical properties of the NNO films we performed contact mode conductive AFM measurements on NNO films deposited onto conductive 1.4 % Nb-doped STO (Nb-STO) substrates.

Fig. 6 presents the current-voltage curves for films with thicknesses of 125 nm and 290 nm (a) and (b), respectively. For the NNO film 125 nm thick, the measurement areas were chosen as "dark" ones, indicated in blue frame on the topography image in Fig. 5a. The loops exhibit the typical FE behavior with two visible current peaks [25]. This I–V hysteresis behavior observed in the 125 nm thin film is primarily attributable to the NNO layer at the substrate interface, which is presumed to exhibit the FE Q phase [32]. Fig. 6b presents measurements on films with thicknesses of 290 nm deposited on Nb-STO, and, in this case, interpreting the I–V curve is more challenging due to the simultaneous contributions from the Q phase, near the substrate, and the overlying P phase. Two different hysteresis loops were observed based on the measurement area: one corresponding to the 3D structures ("light" higher area in the AFM topography image on Fig. 6b, red curve) and the other to the underlying 2D structural layer ("dark" lower area in the AFM topography image on Fig. 6b, blue curve). The displayed I–V curves of this mixed state are characterized by two butterfly-like loops at higher voltages that tend to close at the origin. However, an enlargement of the low voltage-current region, in the inset of Fig. 6b, reveals again behavior typical of FE materials. Moreover, it is evident that in the I–V curve corresponding to the 2D (lower, "dark") region, the FE response is more pronounced, the butterfly wings are less evident, and the FE loop is considerably wider (Fig. 6b, blue line). This dual behavior, coexistence of FE and AFE characteristics, can be explained by the superposition of two contributions in the thicker films, where both the FE Q phase and the AFE P phase coexist.

To confirm this phase assignment at the macroscopic level, we performed the dielectric permittivity measurements as a function of temperature on two representative films grown on NGO(110): a 16 nm fully strained FE Q-phase film and a 160 nm relaxed AFE P-phase film (see Fig. 6c and d, respectively). The in-plane relative permittivity is of the order of 10^2–10^3 in the explored range of temperature in the 16 nm thick film, whereas in the 160 nm thick film it remains below 30 over the same temperature window. Thus, under comparable measurement conditions, the FE Q-phase film is roughly two orders of magnitude more polarizable than the AFE P-phase film. This picture is consistent with Landau–Ginzburg treatments of misfit-strain phase diagrams in epitaxial perovskite films and with first-principles misfit-strain phase diagrams for $NaNbO_3$ [39,40].

The formation of the AFE P phase is a highly complex process that initiates when nucleation centers appear on the surface of the FE Q phase layer. The P phase begins to deposit once the film reaches a

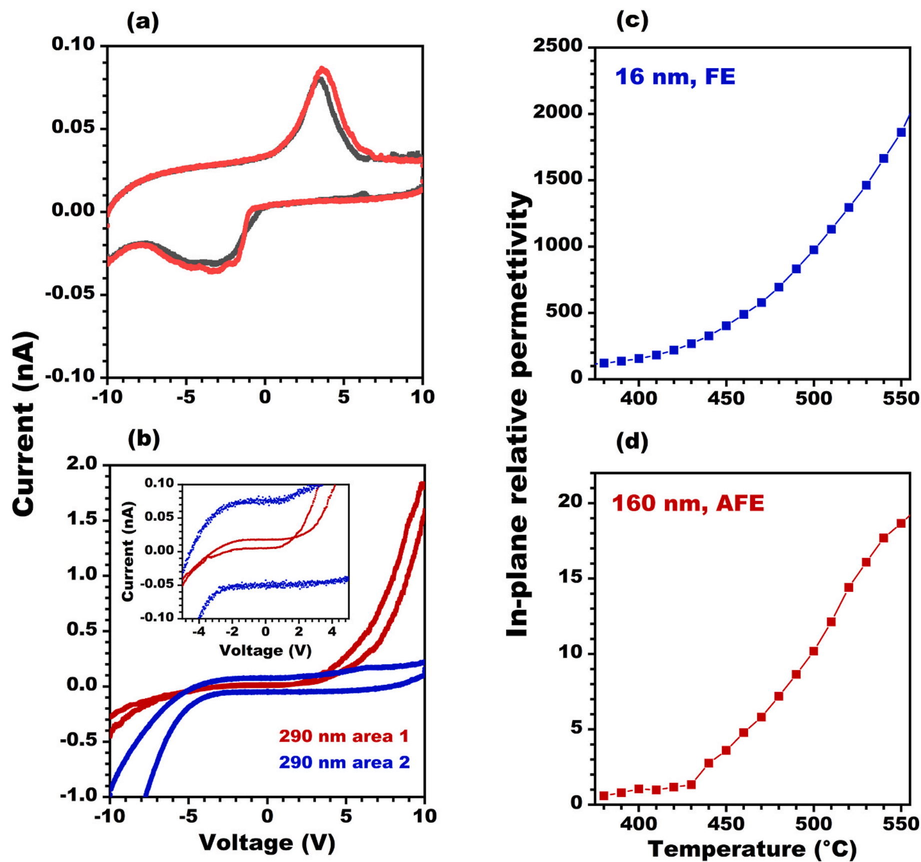

Fig. 6. EIS and conductive-AFM measurements of NNO films grown on 1.4 % Nb-doped STO (001) at 750 °C and partial oxygen pressure of 1 mbar.
(a) I–V curves measured on the "dark" areas of the 125 nm thick film, displaying the double-peak FE behaviour, characteristic of the Q phase; (b) I–V curves acquired on the "light" 3D column (red curve) and on the "dark" area (blue curve) of the 290 nm thick film, showing an AFE-like butterfly loop response for the "light" columns and a FE hysteresis loop for the underlying "dark" area. (c) and (d) represent the in-plane relative permittivity temperature dependence measured at a frequency of 1 kHz on the samples of 16 nm and 160 nm thickness, respectively. (For interpretation of the references to color in this figure legend, the reader is referred to the Web version of this article.)

threshold thickness, which depends on the deposition temperature and decreases with increasing temperature. Moreover, we observed that the onset of the presumed Q-to-P transition varies with the substrate, likely due to differences in strain conditions and interfacial chemistry between the film and the substrate. In particular, this Q-to-P phase transition thickness is lower for films deposited on NGO with respect to STO. Considering that the pseudocubic lattice parameter of NGO (3.875 Å) imposes a larger strain on the NNO film compared to the cubic lattice parameter of STO (3.905 Å), the enhanced strain energy facilitates the earlier growth of the P phase in the case of NNO grown on NGO substrate. These observations are in agreement with the findings of Luo et al. [33].

Based on our findings, we propose that NNO films initially grow in the Q-phase during laser deposition at both 600 °C and 750 °C. Once the films reaches a sufficient thickness, dependent on the substrate and growth temperature, the P phase begins to form as nucleation centers emerging on the film surface. The predominance of the P phase at higher growth temperatures suggests that increased thermal energy promotes the gradual transformation of the Q phase into the P phase. This is consistent with the different contributions of the FE and AFE phases observed in Fig. 6b, which correspond primarily to regions at the bottom and top of the wrinkle-like structures, respectively. These outcomes quantitatively correlate with changes in the concentrations of the Q and P phases in the bulk material [31], due to the thermal energy necessary for the Q-to-P transition. The emergence of the P phase is accompanied by a particular surface morphology: columns of the new phase protrude from the original layer. This can be attributed to the combined effects of increased thermal energy and local strain. The resulting rise in total free energy makes layer wetting unfavorable, leading to island growth between the Q and P phases to minimize the interface. The local strain of the underlying layer can be responsible for the wrinkle-like morphology. Additionally, strain minimization may promote the formation of the AFE phase from the FE phase, as reported by Schneider et al. [6].

4. Conclusions

Our study demonstrates that the NNO thin films deposited at 600 °C exhibit the FE Q phase for thicknesses below 45 nm and the AFE P phase for thicknesses above 45 nm. For a deposition temperature of 750 °C, films initially grow in the Q phase, with thicknesses ranging from 45 nm to 125 nm, depending on the substrate used. Beyond this thickness, the P phase begins to form, suggesting that temperature and substrate-induced strain significantly influence the phase transition. Films grown on STO substrates have a thicker initial Q-phase layer, requiring up to 125 nm before the P phase nucleates at the surface. In contrast, films on NGO substrates show the appearance of the P phase at a thickness of about 45 nm. This lower thickness is due to the combined effect of the thermal energy required for the phase transition from Q to P, and the higher strain energy stored in the NGO-based films. For NNO films on NGO (101), an appropriate choice of deposition temperature produces a fully single-phase layer — either pure Q or pure P — with no detectable mixed domains.

The ability to control phase formation through deposition temperature and substrate selection allows fine-tuning of NNO films' properties,

making them promising for advanced electronic and optoelectronic applications.

CRediT authorship contribution statement

Olga Krymskaya: Writing – review & editing, Writing – original draft, Visualization, Methodology, Investigation, Formal analysis, Data curation, Conceptualization. **Pasquale Orgiani:** Writing – original draft, Visualization, Investigation. **Louis Muse:** Investigation, Writing – review & editing. **Jean-François Blach:** Investigation, Writing – review & editing. **Simone Sanna:** Writing – review & editing, Visualization, Investigation, Conceptualization. **Daniele Di Castro:** Writing – review & editing, Investigation. **Paolo Barone:** Writing – review & editing, Investigation. **Marco Fortunato:** Writing – review & editing, Investigation. **Rachel Desfeux:** Investigation, Writing – review & editing. **Carmela Aruta:** Writing – review & editing, Validation, Supervision, Methodology, Investigation, Funding acquisition, Conceptualization. **Antonello Tebano:** Writing – review & editing, Writing – original draft, Visualization, Validation, Supervision, Project administration, Methodology, Investigation, Funding acquisition, Conceptualization.

Declaration of competing interest

The authors declare that they have no known competing financial interests or personal relationships that could have appeared to influence the work reported in this paper.

Acknowledgements

Research at SPIN-CNR and Olga Krymskaya PhD were supported by the project ECS00000024 "Ecosistemi dell'Innovazione"— Rome Technopole of the Italian Ministry of University and Research, public call n. 3277, PNRR— Mission 4, Component 2, Investment 1.5, financed by the European Union, Next Generation EU.

We acknowledge the national research project "CO_2 Advanced, environmental-friendly nano-technology based electrochemical REduction (CARE)" (Prot. 2022KJ7A47) for financial support.

We also acknowledge Stefano Pergolini, Quantum Design Italy, for the support in the AFM measurements and Maria Sky for the realization of the Graphical Abstract.

Appendix A. Supplementary data

Supplementary data to this article can be found online at https://doi.org/10.1016/j.matchemphys.2026.132010.

Data availability

XRD/RSM datasets and raw AFM images are available from the corresponding author upon reasonable request.

References

[1] R.H. Dungan, R.D. Golding, Metastable Ferroelectric Sodium Niobate, 1964.
[2] A. Xie, J. Fu, R. Zuo, Achieving stable relaxor antiferroelectric P phase in $NaNbO_3$-based lead-free ceramics for energy-storage applications, J. Materiomics 8 (2022) 618–626, https://doi.org/10.1016/j.jmat.2021.11.012.
[3] M.H. Zhang, L. Fulanović, C. Zhao, J. Koruza, Review on field-induced phase transitions in lead-free NaNbO3-based antiferroelectric perovskite oxides for energy storage, J. Materiomics 9 (2023) 1–18, https://doi.org/10.1016/j.jmat.2022.09.008.
[4] H. Qi, G. Wang, Y. Zhang, D. Wang, H. Liu, S. Deng, et al., Tunable phase structure in $NaNbO_3$ ceramics by grain-size effect, electric field and heat treatment, Acta Mater. 248 (2023), https://doi.org/10.1016/j.actamat.2023.118778.
[5] R. Xu, K.J. Crust, V. Harbola, R. Arras, K.Y. Patel, S. Prosandeev, et al., Size-Induced ferroelectricity in antiferroelectric oxide membranes, Adv. Mater. 35 (2023), https://doi.org/10.1002/adma.202210562.
[6] T. Schneider, J. Cardoletti, P. Komissinskiy, L. Alff, Impact of strain engineering on antiferroelectricity in $NaNbO_3$ thin films, ACS Omega 8 (2023) 23587–23595, https://doi.org/10.1021/acsomega.3c01327.
[7] J. Koruza, P. Groszewicz, H. Breitzke, G. Buntkowsky, T. Rojac, B. Malič, Grain-size-induced ferroelectricity in $NaNbO_3$, Acta Mater. 126 (2017) 77–85, https://doi.org/10.1016/j.actamat.2016.12.049.
[8] W. Li, X. Xia, J. Zeng, L. Zheng, G. Li, Significant differences in $NaNbO_3$ ceramics fabricated using Nb_2O_5 precursors with various crystal structures, Ceram. Int. 46 (2020) 3759–3766, https://doi.org/10.1016/j.ceramint.2019.10.098.
[9] U. Farooq, R. Phul, S.M. Alshehri, J. Ahmed, T. Ahmad, Electrocatalytic and enhanced photocatalytic applications of sodium niobate nanoparticles developed by citrate precursor route, Sci. Rep. 9 (2019), https://doi.org/10.1038/s41598-019-40745-w.
[10] Y. Fan, Z. Zhou, R. Liang, M. Zhou, X. Dong, The effect of A-site nonstoichiometry on the microstructure, electric properties, and phase stability of $NaNbO_3$ polycrystalline ceramics, J. Eur. Ceram. Soc. 39 (2019) 4712–4718, https://doi.org/10.1016/j.jeurceramsoc.2019.06.041.
[11] H. Liu, H. Wu, Khuong, P. Ong, T. Yang, P. Yang, et al., Giant piezoelectricity in oxide thin films with nanopillar structure, Science 369 (2020) 292–297, https://doi.org/10.1126/science.abb3209.
[12] B. Lin, K.P. Ong, T. Yang, Q. Zeng, H.K. Hui, Z. Ye, et al., Ultrahigh electromechanical response from competing ferroic orders, Nature (2024), https://doi.org/10.1038/s41586-024-07917-9.
[13] S. Singh, N. Khare, Coupling of piezoelectric, semiconducting and photoexcitation properties in NaNbO3 nanostructures for controlling electrical transport: realizing an efficient piezo-photoanode and piezo-photocatalyst, Nano Energy 38 (2017) 335–341, https://doi.org/10.1016/j.nanoen.2017.05.029.
[14] D. Kumar, S. Sharma, N. Khare, Piezo-phototronic and plasmonic effect coupled Ag-$NaNbO_3$ nanocomposite for enhanced photocatalytic and photoelectrochemical water splitting activity, Renew. Energy 163 (2021) 1569–1579, https://doi.org/10.1016/j.renene.2020.09.132.
[15] A. Bougoffa, A.E. Mabrouki, A. Trabelsi, E. Dhahri, K. Khirouni, Photovoltaic properties of new solar cell based on ideal cubic $NaNbO_3$ thin films: a combined experimental and density functional theory study, RSC Adv. 13 (2023) 30092–30100, https://doi.org/10.1039/d3ra04084d.
[16] S.S.A. Gillani, Mubashra Nazir Ali, Tousif Houssain, M. Shakil, Riaz Ahmad, Urooj Shuaib, et al., Cubic to tetragonal structural phase transformation in $NaNbO_3$ with peculiar Mg and ca doping and its repercussions on optoelectronic properties, Optik 247 (2021) 168017, https://doi.org/10.1016/j.ijleo.2021.168017.
[17] S.A. Khattak, S.M. Wabaidur, M.A. Islam, M. Husain, I. Ullah, S. Zulfiqar, et al., First-principles structural, elastic and optoelectronics study of sodium niobate and tantalate perovskites, Sci. Rep. 12 (2022), https://doi.org/10.1038/s41598-022-26250-7.
[18] J.M. Rosso, E.A. Volnistem, I.A. Santos, T.G.M. Bonadio, V.F. Freitas, Lead-free $NaNbO_3$-based ferroelectric perovskites and their polar polymer-ceramic composites: fundamentals and potentials for electronic and biomedical applications, Ceram. Int. 48 (2022) 19527–19541, https://doi.org/10.1016/j.ceramint.2022.04.089.
[19] M. Xu, L. Lin, G. Jin, Y. Lin, K. Zhang, Two-in-one: portable piezoelectric and plasmonic exciton effect-based co-enhanced photoelectrochemical biosensor for point-of-care testing of low-abundance cancer markers, Biosens. Bioelectron. 211 (2022), https://doi.org/10.1016/j.bios.2022.114413.
[20] Z. Yu, H. Gong, J. Xu, Y. Li, Y. Zeng, X. Liu, et al., Exploiting photoelectric activities and piezoelectric properties of NaNbO3 semiconductors for point-of-care immunoassay, Anal. Chem. 94 (2022) 3418–3426, https://doi.org/10.1021/acs.analchem.2c00066.
[21] G. D'Ambrogio, O. Zahhaf, M.Q. Le, M. Bordet, P. Lermusiaux, N. Della Schiava, et al., Piezoelectric biosensor for smart cardiovascular grafts based on NaNbO3 fibers/PDMS structured composite, Mater. Des. 223 (2022), https://doi.org/10.1016/j.matdes.2022.111195.
[22] Y. Luo, Y. Xiao, J. Liu, Y. Wu, Z. Zhao, Design and application of a flexible nano cardiac sound sensor based on P(VDF-TrFE)/KNN/GR composite piezoelectric film for heart disease diagnosis, Nanotechnology 35 (2024), https://doi.org/10.1088/1361-6528/ad0502.
[23] D. Khare, P. Singh, A.K. Dubey, Interplay of surface polarization charge, dynamic electrical stimulation and compositional modification towards accelerated osteogenic response of NaxK1-xNbO_3 piezo-bioceramics, Biomater. Adv. 140 (2022), https://doi.org/10.1016/j.bioadv.2022.213042.
[24] B. Xu, J. Íñiguez, L. Bellaiche, Designing lead-free antiferroelectrics for energy storage, Nat. Commun. 8 (2017), https://doi.org/10.1038/ncomms15682.
[25] M.H. Zhang, H. Ding, S. Egert, C. Zhao, L. Villa, L. Fulanović, et al., Tailoring high-energy storage NaNbO3-based materials from antiferroelectric to relaxor states, Nat. Commun. 14 (2023), https://doi.org/10.1038/s41467-023-37060-4.
[26] Z. Lv, T. Lu, Z. Liu, T. Hu, Z. Hong, S. Guo, et al., $NaNbO_3$-Based multilayer ceramic capacitors with ultrahigh energy storage performance, Adv. Energy Mater. 14 (2024), https://doi.org/10.1002/aenm.202304291.
[27] S. Aso, H. Matsuo, Y. Noguchi, Reversible electric-field-induced phase transition in Ca-modified NaNbO3 perovskites for energy storage applications, Sci. Rep. 13 (2023), https://doi.org/10.1038/s41598-023-33975-6.
[28] Z. Chen, S. Mao, L. Ma, G. Luo, Q. Feng, Z. Cen, et al., Phase engineering in $NaNbO_3$ antiferroelectrics for high energy storage density, J. Materiomics 8 (2022) 753–762, https://doi.org/10.1016/j.jmat.2022.03.004.
[29] V. Shanker, S.L. Samal, G.K. Pradhan, C. Narayana, A.K. Ganguli, Nanocrystalline $NaNbO_3$ and NaTaO3: rietveld studies, Raman spectroscopy and dielectric properties, Solid State Sci. 11 (2009) 562–569, https://doi.org/10.1016/j.solidstatesciences.2008.08.001.
[30] A.W. Hewat, Neutron powder profile refinement of ferroelectric and antiferroelectric crystal structures: sodium niobate at 22°C, Ferroelectrics 7 (1974) 83–85, https://doi.org/10.1080/00150197408237955.

[31] M. Ahtee, A.W. Hewat, The structures of $Na_{0.98}K_{0.02}NbO_3$ and $Na_{0.90}K_{0.10}NbO_3$ (phase Q) at room temperature by neutron powder diffraction, Acta Crystallogr. A 31 (1975) 846–850.

[32] C.S. Htet, S. Nayak, A. Manjón-Sanz, J. Liu, J. Kong, D.R. Sørensen, et al., Atomic structural mechanism for ferroelectric-antiferroelectric transformation in perovskite $NaNbO_3$, Phys. Rev. B 105 (2022), https://doi.org/10.1103/PhysRevB.105.174113.

[33] R. Xu, et al., Size-Induced ferroelectricity in antiferroelectric oxide membranes, Adv. Mater. 35 (17) (2023) 2210562, https://doi.org/10.1002/adma.202210562.

[34] T. Saito, H. Adachi, T. Wada, H. Adachi, Pulsed-Laser deposition of ferroelectric $NaNbO_3$ thin films, Jpn. J. Appl. Phys. 44 (9) (2005) 6969–6972, https://doi.org/10.1143/JJAP.44.6969.

[35] S. Yamazoe, A. Kohori, H. Sakurai, Y. Kitanaka, Y. Noguchi, M. Miyayama, T. Wada, The effect of $SrTiO_3$ substrate orientation on the surface morphology and ferroelectric properties of pulsed-laser-deposited $NaNbO_3$ films, Appl. Phys. Lett. 95 (2009) 062906, https://doi.org/10.1063/1.3204692.

[36] W.J. Maeng, I. Jung, J.Y. Son, Enhanced ferroelectric polarization in tetragonally strained $NaNbO_3$ thin film on single-crystal Rh substrate, J. Cryst. Growth 349 (2012) 24–26, https://doi.org/10.1016/j.jcrysgro.2012.04.009.

[37] J. Sellmann, et al., Strained ferroelectric $NaNbO_3$ thin films: impact of pulsed laser deposition growth conditions on structural properties, Thin Solid Films 570 (2014) 107–114, https://doi.org/10.1016/j.tsf.2014.09.016.

[38] T. Schneider, J. Cardoletti, P. Komissinskiy, L. Alff, Impact of strain engineering on antiferroelectricity in $NaNbO_3$ thin films, ACS Omega 8 (26) (2023) 23587–23595, https://doi.org/10.1021/acsomega.3c01327.

[39] N.A. Pertsev, A.K. Tagantsev, N. Setter, Phase transitions and strain-induced ferroelectricity in epitaxial thin films, Phys. Rev. B 61 (2000) R825–R829, https://doi.org/10.1103/PhysRevB.61.R825.

[40] K.Y. Patel, J. Íñiguez, S. Prosandeev, L. Bellaiche, Properties of (001) $NaNbO_3$ films under epitaxial strain: a first-principles study, Phys. Rev. B 103 (2021) 094103, https://doi.org/10.1103/PhysRevB.103.094103.

[41] Yu I. Yuzyuk, R.A. Shakhovoy, S.I. Raevskaya, I.P. Raevski, Marssi M. El, M. G. Karkut, P. Simon, Ferroelectric Q-phase in a $NaNbO_3$ epitaxial thin film, Appl. Phys. Lett. 96 (22) (2010) 222904, https://doi.org/10.1063/1.3437090.

[42] R.A. Shakhovoy, S.I. Raevskaya, L.A. Shakhovaya, D.V. Suzdalev, I.P. Raevski, Y. I. Yuzyuk, A.F. Semenchev, Marssi M. El, Ferroelectric Q and antiferroelectric phases' coexistence and local phase transitions in oxygen-deficient $NaNbO_3$ single crystal: Micro-raman, dielectric and dilatometric studies, J. Raman Spectrosc. 43 (8) (2012) 1141–1145, https://doi.org/10.1002/jrs.3140.